GEOMATICS AND ENVIRONMENTAL ENGINEERING • Volume 20 • Number 5 • 2026

https://doi.org/10.7494/geom.2026.20.5.91

Spatiotemporal Assessment of Hydroclimatic Change and Environmental Vulnerability in Central and Southern Iraq Using Geospatial Techniques

Alaa G. Khalaf[1]*, Raad A. Abbood[1], Imzahim A. Alwan[2], Abdulrazzak T. Ziboon[3]

[1] Scientific Research Commission, Baghdad, Iraq
[2] University of Technology, Civil Engineering College, Baghdad, Iraq
[3] Al Esraa University, Engineering College, Baghdad, Iraq
* Corresponding author

Abstract: Climate and hydrology-related stresses arise in central and southern Iraq as a result of both the impacts of climate change and declining river flows, and long-term assessments are still limited. This study aims to address two questions: how have climatic and environmental conditions changed over time in the study area, and what is the relationship between climate change and drought in the region. A Geographic Information System (GIS) with remote sensing data was utilized to study climatic, hydrological, and ecological variables. The Mann–Kendall test and Sen's slope estimator were used for trend analysis. To assess the vegetation and surface water conditions, the Vegetation Condition Index (VCI) and Normalized Difference Water Index (NDWI) were utilized. The final results illustrated a strengthening pattern of hydroclimatic stress, with a significant decline in rainfall alongside a rise in mean temperature and land surface temperature, which led to increased evaporation rates and declined relative humidity. The surface water decreased from 22 to 15% and the percentage of land affected by extreme drought expanded from 37 to 43%. Also, growing winds and dust storm events underscore a self-enhancing feedback mechanism associated with land degradation. These changes are further intensified by declining inflows from the Tigris and Euphrates rivers because of upstream control over these river systems.

Keywords: geostatistics, Geographic Information System (GIS), Mann–Kendall, Normalized Difference Water Index (NDWI), Vegetation Condition Index (VCI)

Received: February 19, 2026; accepted: June 9, 2026

E-mails and ORCID IDs: alaa.gh.khalaf@src.edu.iq, https://orcid.org/0009-0006-2662-2547 (A.G.K.); raad.a.abbood@src.edu.iq, https://orcid.org/0000-0002-0871-0600 (R.A.A.); 40164@uotechnology.edu.iq, https://orcid.org/0000-0002-8128-6658 (I.A.A.); dr.abdulrazzak@esraa.edu.iq, https://orcid.org/0000-0003-1787-8779 (A.T.Z.).

1. Introduction

Climate change describes a long-term change in the average weather patterns in many regions across the Earth and globally over multiple decades or longer. This can be manifested through average climatic conditions changes and through changes in the statistical distribution frequencies of weather events [1]. Climate change is among the most prominent challenges beleaguering Iraq, as it translates into a decrease in cropland, fluctuation of water availability, and negative health outcomes due to drought [2]. Iraq is marked by dry climatic conditions that expose it to the risk of climate change effects and make it one of the most highly sensitive countries in terms of variability in different climatic parameters such as temperature and precipitation [3]. Long-term climate change can affect the frequency and intensity of wildfires, which release large amounts of smoke and particulate matter into the atmosphere, and therefore correlate with air pollution deterioration and human-health effects [4]. Climate change affects worldwide economies and societies through extreme episodes of climatic hazards, water quality deterioration, and rising trends in temperatures [5]. Iraq in Southwest Asia is situated in the northern part of the Arabian Peninsula. Its distance from the major water bodies that have a notable impact on the climatic characteristics of the country is determined by its geographic position. The climate of Iraq occupies a semi-arid region, where rainfall is mostly concentrated during the winter and spring seasons, while the summers are dry [6]. The annual rainfall in Iraq shows a direct spatial gradient from less than 100 mm in the southern regions of the country to about 1,200 mm in the northeast, with the winters being cool to cold, while the summers are mainly dry and hot – hot or extremely hot – due the semi-arid climatic conditions that prevail over a large part of the national territory [7]. Satellite remote sensing provides an overview of the Earth's surface and valuable information, making it a powerful means for studying spatial distribution and temporal dynamics in climate change as well as phenomena such as drought [8]. Remote sensing is an alternative to traditional surveys which uses satellite data to provide a variety of spatial information including urbanizing regions, land use and cover type, green space distribution maps (GS), water body charts, etc. [9].

2. Literature Review

The spatiotemporal dynamics of climate, hydrology, and vegetation have been well studied under a variety of ecological settings. For example, Al-Timimi and Al-Khudhairy [10] studied long-term variations in maximum surface air temperature using meteorological stations over the period 1980–2015 for Iraq. The Mann–Kendall statistical method they used showed significant warming trends in all seasons, with the highest temperatures observed during summer months – limited to the south of their study site – and progressively lower temperature values toward its north. Vegetation affected by environmental variability was analyzed by Mzuri et al. [11], who evaluated vegetation changes in the Duhok area from 2000 to 2019 by Landsat images and the Modified Soil Adjusted Vegetation Index with climatic and terrain-related variables. They found that the improved vegetation conditions in northern mountainous regions contrasted with declining vegetation cover in low-elevation regions, largely influenced by rainfall, elevation, temperature, slope, and aspect. In the same line of work, Aljuhaishi et al. [12] analyzed near-daily atmospheric circulations over Iraq for 1999–2020 and highlighted five dominant circulation systems, indicating significant season–spatial variation, such as more summer monsoonal low-pressure systems in southern parts of the country compared to those in the north under the Siberian high that predominates during winter. Al-Maliki et al. [13] explored future climate trajectories using statistically downscaled climate projection scenarios that predicted significant warming and uncertain climatic trends for rainfall at the end of the twenty-first century and beyond, indicating as much drought and thus likely more water stress. In addition, Muter et al. [14], using MODIS NDVI data from 2000 to 2021, evaluated spatiotemporal trends of vegetation cover across Iraq and illustrated significant spatial/temporal variability in greenness; a low positive correlation with rainfall; more abundant vegetation cover was found in the humid northern and eastern regions, while central areas illustrated a substantial declining trend consistent with decreased rainfall as well as ever-expanding urbanization. Also, Alemu [15] analyzed long-term precipitation and temperature trends in Dessie Zuria from 1981 to 2022, utilizing the Mann–Kendall test and Sen’s slope estimator to assess regional climate change. He highlighted high monthly precipitation variability and a general rise in thermal indices, confirming the local impact of global climate shifts.

Spatial interpolation using GIS has been widely applied in environmental and climatic studies, and cross-validation is usually used to assess the predictive performance and reliability of interpolation models by comparing observed and predicted values. For example, Radić et al. [16] investigated the effectiveness of several interpolation models for predicting wind speed and direction at unknown locations based on a network of climate stations (distributed across the Split–Dalmatia County). They used the natural neighbor interpolation, inverse distance weighting (IDW), kriging, and ordinary kriging methods. Finally, they concluded that ordinary kriging has the lowest prediction error compared to the other methods. Meanwhile, Feng et al. [17] used interpolation methods such as kriging, IDW, and the spline to obtain a spatial distribution map of air temperature for Jiangxi Province based on weather stations. According to cross-validation, they concluded that the kriging method was more suitable for the spatial interpolation of temperatures in the study area. Also, Pandey et al. [18] performed spatial interpolation techniques on rainfall data to predict the unspecified values in the Bisalpur catchment. They used six interpolation models: natural neighbor, IDW, Trend, Spline, kriging, and topo to raster. They concluded that the geostatistical interpolation (kriging and topo to raster) methods produced better results than other models because they are based on the spatial variability of data.

The large body of research focused on vegetation dynamics and climate variability has not yet led to distinct improvements of our understanding about climate–environment interactions as previous studies have typically relied on either one or a few variables-based analyses or cover relatively small zones or have separately looked at isolated data sources. Especially in the highly vulnerable regions, few studies have explored integrated influences across a number of climatic variables (temperature, rainfall, humidity, evaporation, wind speed, or dust storm activity) on plant or water area. This identified a clear research gap in the absence of an integrated, multi-source framework that describes the systematic relationship between climatic stressors and ecological responses over longer timeframes. To fill this gap, the present study employs a combination of ground-based observations and satellite datasets within a GIS framework with statistical techniques for performing a spatially explicit spatiotemporal assessment of hydroclimatic variability in central and southern Iraq together with environmental vulnerability during the period from 2001 to 2024.

Thus, this study aims to address the following research questions:

1) How have climatic and environmental conditions changed over time in the study area?
2) What is the relationship between climate change and drought in the region?

These questions lead us to hypothesize that the broad study area has transitioned to greater aridity and environmental susceptibility, with climatic changes directly driving increases in drought and ecological deterioration.

3. The Study Area

The Central and Southern region of Iraq, which extends over about 165,282 km^2 and is located between latitudes 29°0′0″N and 33°0′0″N and longitudes 43°0′0″E and 49°0′0″E, was selected to be the study area. It consists of parts of nine governorates, which are Qadissiya, Babylon, Kerbala, Najaf, Thi Qar, Wassit, Missan, Basrah, and Muthanna (see Fig. 1). In recent decades, Iraq has experienced increasing climatic variability and recurrent droughts, causing significant environmental and socio-economic impacts. These include loss of arable land, water supply instability, population displacement, reduced soil fertility, marshland shrinkage, groundwater depletion, and intensified dust storms, particularly in the central and southern regions. These areas are vital agricultural zones with substantial economic importance but continue to face challenges from climate change, water scarcity, and declining crop yields. Despite these issues, few studies have utilized remote sensing and GIS to investigate climate-related phenomena in these regions.

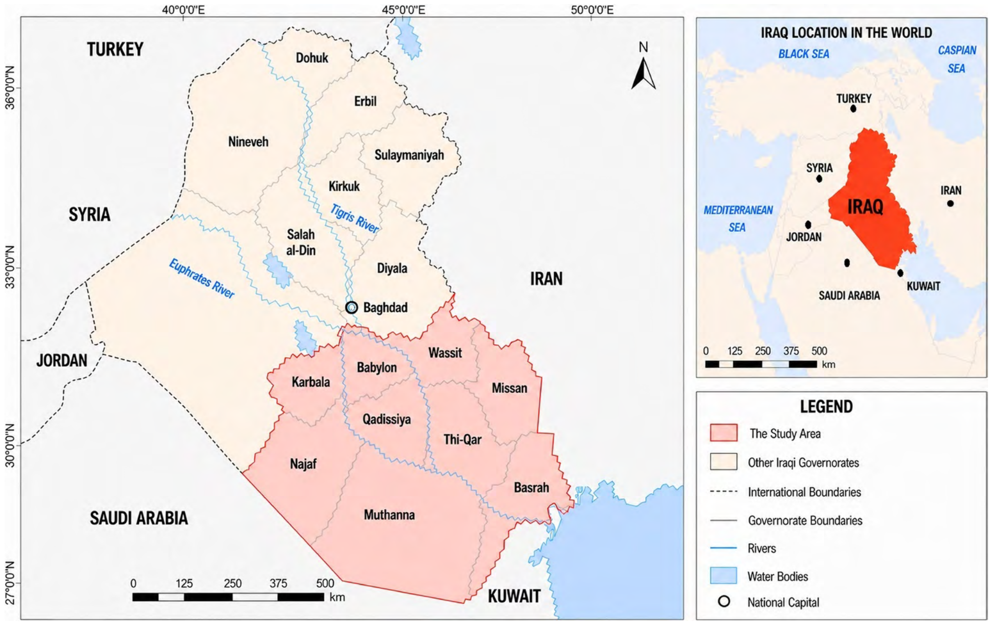

Fig. 1. A location map illustrating the study area in Iraq.
The map highlights central and southern governorates within Iraq,
displays neighboring countries, and includes major geographic features
such as water bodies, rivers, administrative boundaries,
and an inset map showing Iraq's location in the world

Source: own elaboration based on [19]

4. Research Methods

4.1. Data Used and Methodology

This study used a range of climatic variables, such as mean monthly temperature, rainfall, relative humidity, evaporation rate, wind speed/direction, and dust storm event frequency. Climate data were collected using a two-source approach. Evaporation and dust storm measurements were obtained from the primary source, which was the Iraq Meteorological and Seismological Organization. To fill in time gaps occurring at local stations, in particular from 2003 to 2006, the other climate variables were extracted from the NASA Power database [20] in CSV format. The study area consists of nine climate observation stations: Qadissiya, Babylon, Kerbala, Najaf, Thi Qar, Wassit, Missan, Basrah, and Muthanna. MODIS imagery [21] over the same time was also used to calculate the Vegetation Condition Index (VCI), and Normalized Difference Water Index (NDWI), while Land Surface Temperature (LST) data were extracted from MODIS/Terra 8-Day L3 Global 1km. All spatial analyses and map production were performed in the ArcGIS 10.4 program. The implemented spatial interpolation procedures (specifically kriging) were performed using the Geostatistical Analyst extension, which converted point-based meteorological observations into continuous spatial climate surfaces. The interpolated outputs provided a means to map climatic irregularities, hotspots, and the distribution of areas exposed to climatic extremes. In parallel, temporal analyses were performed to identify interannual variability and recent hydroclimatic variability behavior across the study region. The presence of statistically significant monotonic trends was determined using the non-parametric Mann–Kendall test, and Sen's slope estimator was used to compute both the magnitude and direction of change using the RStudio program. Figure 2 illustrates the methodology that was applied in this study.

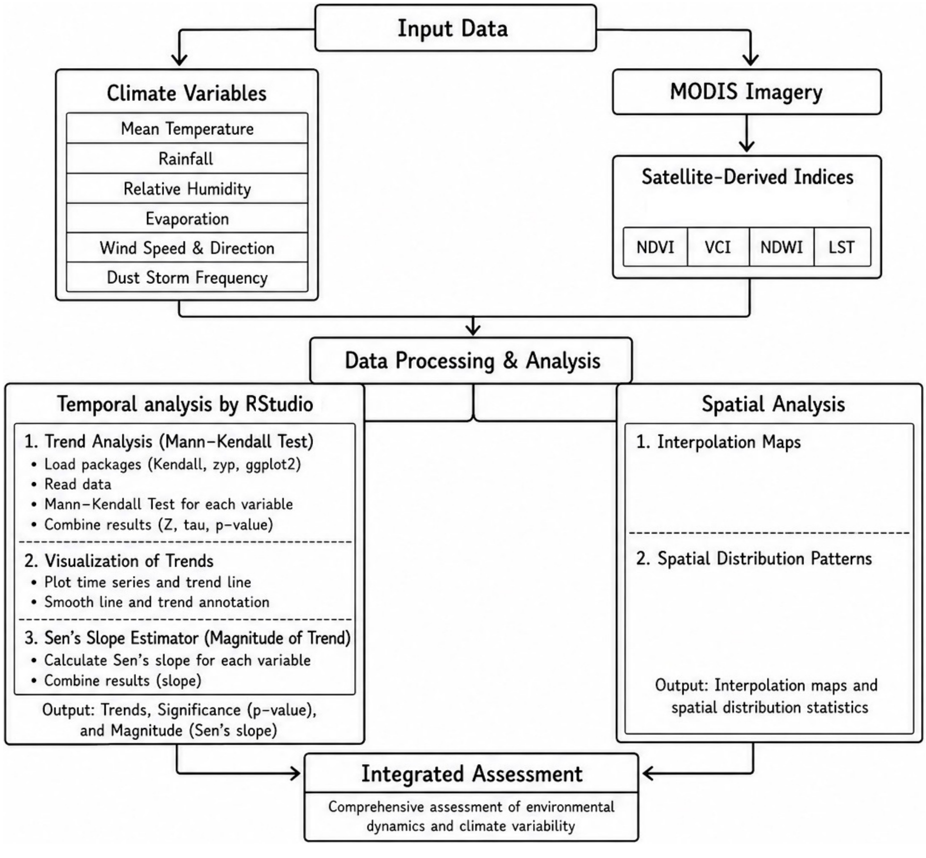

Fig. 2. Flowchart of methodology work

4.2. Geostatistical Analyst to Produce Climatic Maps

Geostatistical analysis is a statistical discipline that deals with spatial or spatiotemporal datasets. This approach works based on a semivariogram, which is an object used to quantify the level of spatial correlation between tuples. The semivariogram plots the variance of differences between pairs of observations against the distance separating them, providing a measure of dependence in space. This relationship is essential in geostatistical interpolation because it makes it possible to predict the values of other unsampled locations. Modeling the spatial dependence using the semivariogram assists in determining the weights assigned to the observed data, which leads to more precise predictions of locations where data were not measured [22]. Interpolation can be classified into two main broad types: deterministic and geostatistical methods. Deterministic interpolation methods, such as inverse distance weighting (IDW) and Thiessen polygons, attribute values to locations based on the neighboring observed values and mathematical equations that determine how smooth the created surface is. Geostatistical approaches such as kriging are based on statistical models prone to autocorrelation [23]. In the present study, ArcMap 10.4 was utilized to create continuous spatial distribution maps of the climate from point-based data, including both measured and predicted samples. The interpolation was carried out using the kriging method. This approach is at its core founded on the notion of spatial autocorrelation, described by a variogram model. Instead of only the observed values, this model describes the spatial dependence structure within the data. Once a robust variogram model is established, the optimal interpolation weights are calculated with a data-driven process. It aims to reduce the variance of prediction by minimizing the estimation of the bias using the following weights [24]. Mathematically, the predicted value at a specific location (u) can be expressed as follows [25]:

$$z(u) = \sum_{\alpha=1}^{n} \lambda_{\alpha}(u) z(u_{\alpha}) \tag{1}$$

In the model, a random variable at a certain location u_α is represented as $z(u_\alpha)$. The n data locations are indicated by u_α, ordinary kriging weights represented by $\lambda_\alpha(u)$, and the predicted value by $z(u)$. And here, $\lambda_\alpha(u)$ is in the process of being weighed. Instead of just considering the distance from the sample points to the prediction location as a basis for the weighting, these scales also consider the overall spatial distribution of the measured data. To use the spatial distribution in weighing, the spatial autocorrelation must first be quantified. Therefore, in ordinary kriging, the weight, $\lambda_\alpha(u)$ depends on a model fitted to the points measured, the distance to the prediction location, and the spatial relationships between the measured values around the prediction location [25].

In this study, the ordinary kriging method was adopted as a geostatistical interpolation technique based on cross-validation and numerous previous studies that have demonstrated its efficiency in representing and analyzing climatic data. This method relies on statistical modeling of the spatial correlation among observed values, which contributes to improving the accuracy of estimating values in unmeasured locations. The studies by Batool et al. [26], Jannah et al. [27], and Jang et al. [28] highlighted the effectiveness of kriging in environmental and climatic data analysis.

4.3. Vegetation Condition Index (VCI)

For this study, the VCI was calculated using the NDVI values obtained from MODIS (8-day 500-meter surface reflectance data (MOD09A1, Collection)) satellite data to compare drought conditions determined by analyses conducted for the study area. Accordingly, the VCI time series was obtained using satellite data covering the years 2001–2024 for each 500 m satellite cell within the study area boundaries. The VCI-based drought metric equation was developed into a global drought watch system using VCI derived from NDVI data. The VCI was calculated by applying the following equation to the final NDVI data [29]:

$$\mathrm{VCI} = \frac{(\mathrm{NDVI}_i - \mathrm{NDVI}_{\min})}{(\mathrm{NDVI}_{\max} - \mathrm{NDVI}_{\min})} \cdot 100 \tag{2}$$

where NDVI_i is the NDVI value of the pixel during a specific year i, and $\mathrm{NDVI}_{\max}$ and $\mathrm{NDVI}_{\min}$ are the maximum and minimum NDVI values.

The maximum and minimum values of the denominator reflect the best and worst conditions of vegetative growth, and the difference between them somewhat reflects the condition of the local vegetation. The VCI contains both real-time and historical information of the NDVI. The VCI ranges between 0 and 100, in which smaller VCI values indicate worse vegetation growth and higher degrees of drought [29]. The VCI describes the spatial and temporal variations in vegetation cover and indicates the impact of weather on vegetation. High VCI values indicate non-drought or healthy vegetation conditions, while values close to zero indicate severe drought. VCI values below 35% denote drought conditions, while values near 50% or higher indicate normal or relatively good thermal conditions [30].

4.4. Normalized Difference Water Index (NDWI)

The utilization of remote sensing data in the field of environmental hydrology is experiencing rapid progress. The NDWI is an algorithm used to detect water bodies with the capacity to absorb visible and infrared wavelengths strongly. It is a popular index used for identifying humidity and dryness [31]. It is formulated as a numerical indicator generated using mathematical expressions such as band ratio calculations. A classification threshold is then applied to this indicator to enable the separation of aquatic features from non-water surfaces based on their distinct spectral responses. By exploiting absorption properties, the applied mathematical transformations enhance the contrast between water and surrounding land features while concurrently reducing the influence of systematic noise. Such noise commonly arises from sensor-related uncertainties and external environmental factors, including illumination variability, soil background effects, surface topography, and atmospheric interference [32]. MODIS 8-day 500-meter surface reflectance data

(MOD09A1 Collection) were used to extract NDWIs in this study based on the following formula [33]:

$$\mathrm{NDWI} = \frac{(Green - NIR)}{(Green + NIR)} \tag{3}$$

where *Green* and *NIR* are the green and near-infrared bands of a MODIS image. In general, the NDWI ranges from −1 to +1, and theoretical threshold values for this index greater than 0 indicate water bodies in the study area.

4.5. Mann–Kendall (MK) Test

The Mann–Kendall test is one of the most important non-parametric tests used by researchers, especially in the study of trends in climatic elements. One of the advantages of this test is that it is non-parametric and does not require a normal distribution of data. Moreover, in the case of inhomogeneous time series data analysis, having low sensitivity to sudden breaks is the second most important advantage of the test. According to the null hypothesis (H0) of the test, there is no trend, and the data are randomly and independently ordered. The judgement of the null hypothesis is tested by the alternative hypothesis (H1), which assumes the existence of a trend [34]. The Mann–Kendall test statistic is calculated as [35]:

$$S = \sum_{i=1}^{n=1} \sum_{j=i+1}^{n} \mathrm{sign}(x_j - x_i),\ \ \mathrm{sign}(x_j - x_i) = \begin{cases} +1, & \text{if } (x_j - x_i) > 0 \\ 0, & \text{if } (x_j - x_i) = 0 \\ -1, & \text{if } (x_j - x_i) < 0 \end{cases} \tag{4}$$

A positive S value indicates an upward trend, while a negative value indicates a downward trend. The variance of the variable is calculated to obtain the z-value. The variance (S) is computed as:

$$Var(S) = \frac{n(n-1)(2n+5) - \sum_{t=1}^{m} t_i(t_i - 1)(2t_i + 5)}{18} \tag{5}$$

A tied group (m) is a set of variable data with the same value when the sample size is $n > 10$. The normal Z test statistic is calculated by the equation:

$$Z = \frac{S \pm 1}{\sqrt{Var(S)}} \tag{6}$$

This equation uses $S - 1$ if $S > 0$, $S + 1$ if $S < 0$, and Z is 0 if $S = 0$. A positive value of Z indicates an increasing trend. Otherwise, it indicates a downward trend [35].

4.6. The Test of Sen's Slope Estimator

This is one of the most frequently used models for linear trend identification. This method requires, however, the assumption of residual normality. The Sen's slope estimator is found to be a powerful tool for developing linear relationships. Sen's slope has the advantage over the slope of regression in the sense that gross data series errors and outliers do not affect it significantly. The slope of the Sen was determined to be the mean of all pairwise slopes for any pair of points in the dataset. The following equation is used to estimate each individual slope (*mij*) [36]:

$$mij = \frac{Y_j - Y_i}{j - i} \tag{7}$$

where Y_j and Y_i are data values at time j and i ($j > i$), respectively. If there are n values of Y_j in the time series, estimates of the slope will be $N = n\ (n - 2)/2$. The slope of the Sen estimator is the mean slope of such sloped N values. Sen's slope is:

$$M = \begin{Bmatrix} m_{\left|\frac{n+1}{2}\right|} & \text{if } n \text{ is odd} \\ \frac{1}{2}\left(m_{\frac{n}{2}} + m_{\left|\frac{n+2}{2}\right|}\right) & \text{if } n \text{ is even} \end{Bmatrix} \tag{8}$$

A positive Sen's slope indicates an upward trend, while a negative Sen's slope indicates a downward trend.

4.7. Spatial Autocorrelation Analysis

Spatial autocorrelation helps in the understanding of the correlation between a single variable at a location and its values in a relatively close or adjacent location in a two-dimensional space [37]. Moran's *I* is one of the important measures in detecting the spatial autocorrelation between the elements of the phenomenon studied and determining whether the pattern of the spread of the phenomenon is dispersal, regular, or random [38]. Global Moran's *I* [39] was used as the first measure of spatial autocorrelation. Its values range from −1 to 1. The value "1" means a perfect positive spatial autocorrelation (high values or low values cluster together), while "−1" suggests a perfect negative spatial autocorrelation (a checkerboard pattern), and "0" implies perfect spatial randomness [40]. Moran's *I* is the cross-product between the observed variable and its spatial lag, weighted based on its spatial weight in the matrix [37]:

$$I = \frac{\sum_i \sum_j w_{ij} z_i \cdot \frac{z_j}{S_0}}{\frac{\sum_i Z_i^2}{n}} \tag{9}$$

wherein for an observation in the spatial unit i and its neighbor j, $z_i = (x_i - \overline{x})$, where $\overline{x}$ is the mean of variable x, $S_0 = \sum_i \sum_j w_{ij}$ is the sum of all the spatial weights, and n is the number of observations.

5. Results

5.1. Exploratory Data Analysis (EDA)

In this research, an EDA was conducted for all climatic data, which was used to assess whether the data are, in fact, suitable for spatial modeling and which type of modeling is suitable to represent the data. Because of the extensive volume of the collected climatic data, rainfall was selected as an example to show the procedures that were used for the EDA analysis. The results indicated the suitability of the dataset for geostatistical modeling. The histogram (Fig. 3) indicated robust distributional characteristics, with a mean of 118.28, a median of 108.85, and a kurtosis value of 2.92, which closely aligns with the ideal normal distribution value of 3.0.

This normality was further supported by the normal Q-Q plot (Fig. 4), which illustrated a consistent linear alignment of data points along the reference axis. From a spatial perspective, the Voronoi map (Fig. 5) demonstrated a smooth color gradient across all stations in the study area, confirming the absence of significant local outliers.

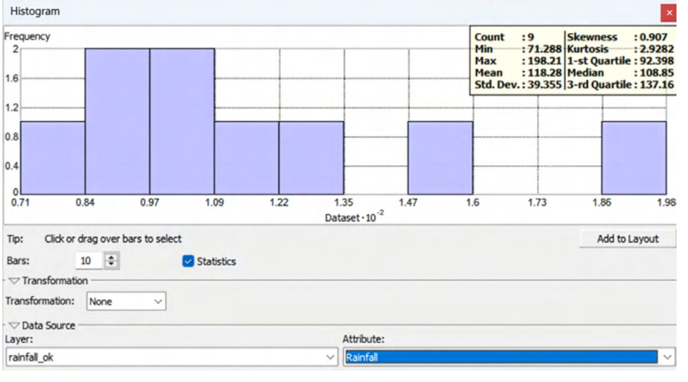

Fig. 3. Histogram of rainfall data

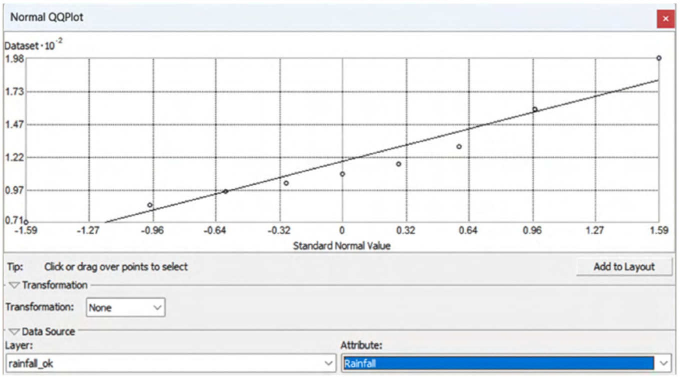

Fig. 4. Normal Q-Q plot of rainfall data

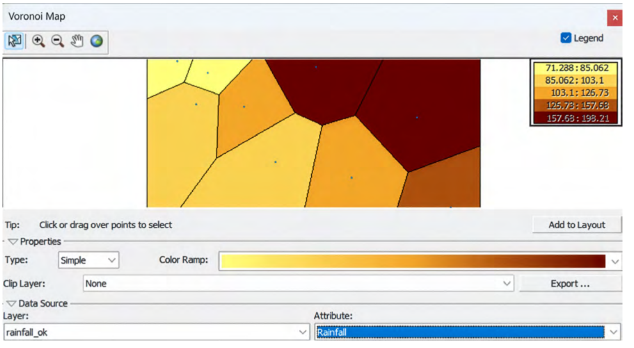

Fig. 5. Voronoi map for spatial outlier detection

Also, the trend analysis (Fig. 6) showed a clear global trend following a specific spatial curve. Finally, the semivariogram/covariance cloud, as illustrated in Figure 7, provided definitive evidence of strong spatial autocorrelation, modeled utilizing a lag size of 0.3619 with 10 lags. In the same way, these procedures were repeated for the other climatic data that were used.

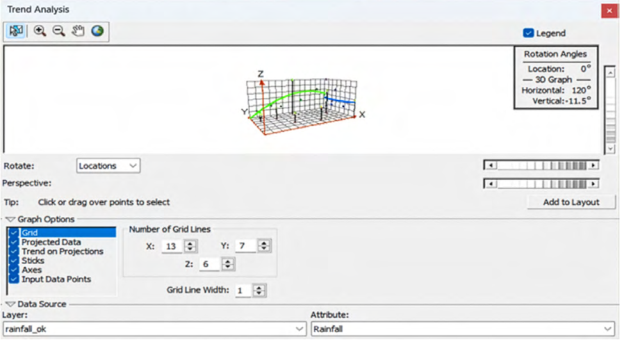

Fig. 6. Trend analysis of rainfall data

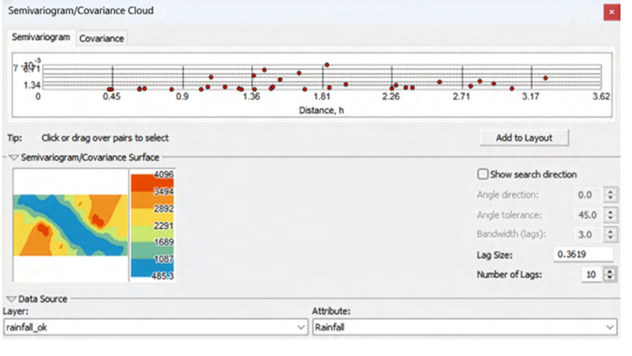

Fig. 7. Semivariogram and covariance cloud and surface

5.2. Spatial Autocorrelation Results

To verify the spatial structure of the climatic variables and satisfy the essential assumptions of geostatistical interpolation, a global Moran's *I* test was performed, as illustrated in Table 1. The results showed that all variables exhibit positive Moran's *I* values. The calculated *z*-values exceeded the threshold of 1.96, while the *p*-values were significantly lower than the standard ($\alpha = 0.05$). This indicated a statistically significant spatial clustering pattern. Geographically, this confirmed that high values tend to cluster near high values, and low values cluster near low values in adjacent climate stations. Regarding dust storms, they have a positive Moran's *I* of 0.2409 and a *z*-value of 1.7158, establishing statistical significance at a 90% confidence level ($p = 0.086 < \alpha = 0.10$). These results indicated that the data are spatially correlated.

Table 1. Results of spatial autocorrelation for the climatic variables

Climatic variable	Moran's *I*	*z*-score	*p*-value	Expected index	Variance
Rainfall rate	0.376759	2.321344	0.020268	−0.125000	0.046721
Mean temperature	0.592694	3.244224	0.001178	−0.125000	0.048939
Evaporation	0.306938	2.030756	0.042280	−0.125000	0.045241
Relative humidity	0.424934	2.409078	0.015993	−0.125000	0.052110
Dust storm	0.240938	1.715885	0.086183	−0.125000	0.045482
Wind speed	0.632254	3.270958	0.001072	−0.125000	0.053596
Wind direction	0.568423	2.941858	0.003262	−0.125000	0.055559

Note: All spatial autocorrelation parameters were calculated utilizing the global Moran's *I* tool in the ArcGIS program. Spatial relationships were determined by the inverse Euclidean distance method, utilizing a standardized distance threshold of 133,268 m for all datasets.

5.3. Assessment of Performance of Interpolation Method

The spatial interpolation was performed using ordinary kriging, which belongs to the geostatistical family of methods. This method was selected for its ability to provide the best linear unbiased prediction by accounting for spatial autocorrelation. To evaluate the performance of the interpolation method, cross-validation was used within the ArcGIS program. The geostatistical wizard was used to refine the model. The semivariogram variable was chosen with four ordinary kriging models: circular, spherical, exponential, and Gaussian. The search neighborhood was defined as standard circular, incorporating a sectoring scheme to ensure a balanced distribution of sampled points. These parameters were selected to ensure that the spatial variability of the climate data is represented with acceptance statistical confidence.

Based on the cross-validation results for ordinary kriging models, the Gaussian model appeared to be the most acceptable spatial interpolation method for all climatic variables evaluated (rainfall rate, relative humidity, evaporation, mean temperature, dust storms, wind speed, and wind direction), as it outperformed the circular, spherical, and exponential models, as shown in Table 2 and Figures 8–14. It showed acceptable predictive accuracy with the lowest bias compared with the other models because it had lower values of mean error (ME), root mean square error (RMSE), and average standard error (ASE). Furthermore, the mean standardized error (MSE) values were closest to zero. In addition to this, its root mean square standardized (RMSS) error was frequently near or closest to the ideal value of one, supporting that it provided the most acceptable spatial interpolation for these data. The final results of the assessment with the spatial autocorrelation analysis provided a methodological justification for replacing the other approaches with the Gaussian interpolation model to ensure unbiased and acceptable spatial predictions for all studied climatic variables across the study region.

Table 2. Cross validation results of ordinary kriging interpolation models

Variable	Model	ME	RMSE	MSE	RMSS	ASE
Rainfall rate	circular	−5.057	29.956	−0.058	0.695	35.557
	spherical	−5.444	30.456	−0.065	0.670	36.758
	exponential	−6.005	31.541	−0.078	0.688	37.978
	Gaussian	−4.390	26.338	−0.067	0.702	31.735
Evaporation	circular	4.215	18.540	0.094	0.742	29.850
	spherical	4.486	18.920	0.102	0.736	30.140
	exponential	4.732	19.380	0.115	0.728	30.620
	Gaussian	3.761	16.249	0.080	0.824	26.416
Relative humidity	circular	1.072	3.485	0.139	0.827	4.128
	spherical	1.108	3.364	0.148	0.815	4.137
	exponential	1.159	3.449	0.152	0.824	4.132
	Gaussian	0.992	2.500	0.126	1.099	2.623

Table 2. cont.

Variable	Model	ME	RMSE	MSE	RMSS	ASE
Mean temperature	circular	−0.038	0.630	−0.022	0.765	0.850
	spherical	−0.040	0.633	−0.024	0.766	0.852
	exponential	−0.063	0.633	−0.040	0.775	0.863
	Gaussian	−0.012	0.595	−0.004	0.786	0.782
Wind direction	circular	0.287	6.977	0.046	0.783	6.926
	spherical	0.298	6.970	0.051	0.772	6.964
	exponential	0.434	6.946	0.064	0.750	7.170
	Gaussian	0.199	6.738	0.034	1.011	6.694
Dust storm	circular	0.142	1.041	0.091	0.870	0.991
	spherical	0.167	1.045	0.099	0.884	0.925
	exponential	0.168	1.055	0.107	0.867	0.981
	Gaussian	0.079	0.586	0.081	1.003	0.628
Wind speed	circular	−0.219	0.678	−0.105	0.863	0.793
	spherical	−0.224	0.680	−0.110	0.864	0.795
	exponential	−0.234	0.656	−0.112	0.853	0.848
	Gaussian	−0.103	0.642	−0.086	1.019	0.668

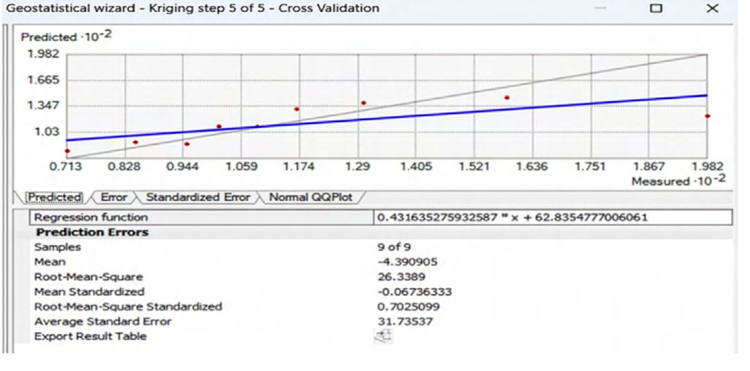

Fig. 8. Comparison of observed and modeled rainfall rate distributions over the study area in 2001–2024

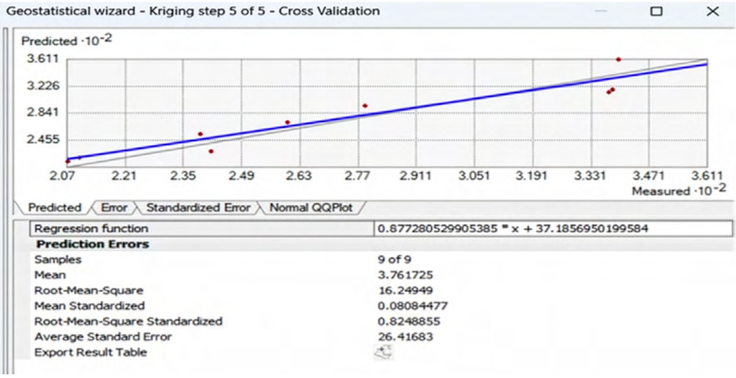

Fig. 9. Comparison of observed and modeled evaporation distributions over the study area in 2001–2024

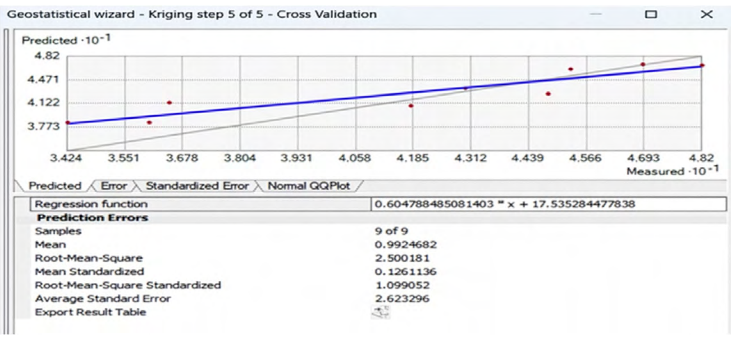

Fig. 10. Comparison of observed and modeled mean of relative humidity distributions over the study area in 2001–2024

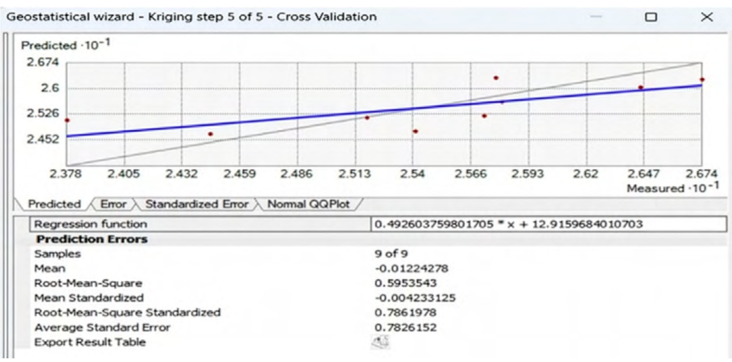

Fig. 11. Comparison of observed and modeled mean temperature distributions over the study area in 2001–2024

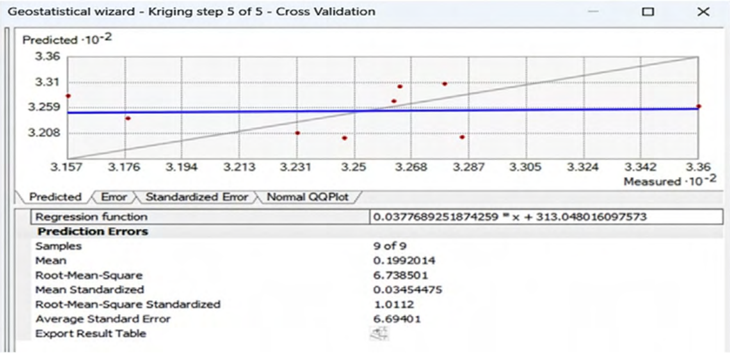

Fig. 12. Comparison of observed and modeled wind direction distributions over the study area in 2001–2024

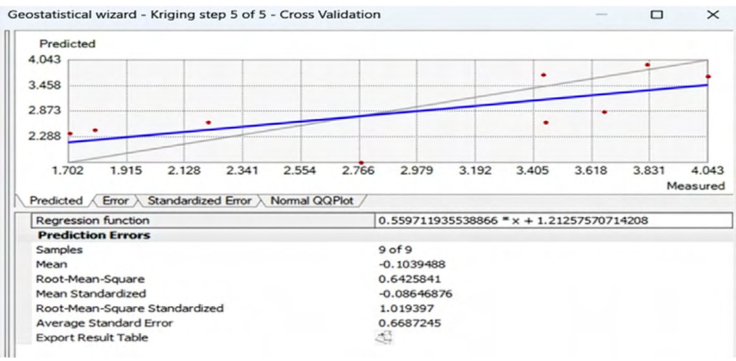

Fig. 13. Comparison of observed and modeled wind speed distributions over the study area in 2001–2024

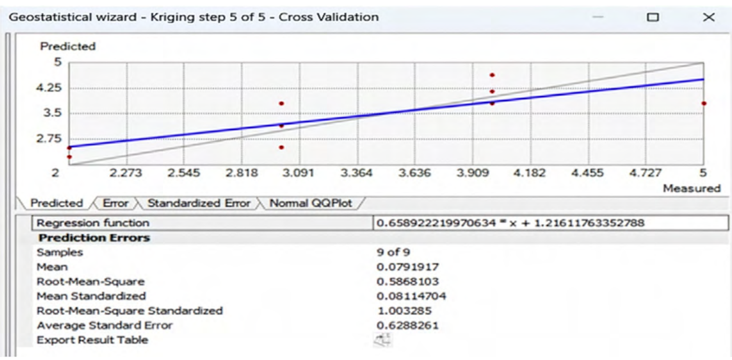

Fig. 14. Comparison of observed and modeled mean of dust storm distributions over the study area in 2001–2024

5.4. Spatiotemporal Dynamics of Climate, Water, and Vegetation Variability in the Study Area (2001–2024)

Rainfall Trend and Spatial Variability

The results of the Mann–Kendall test and Sen's slope estimator for the period 2001–2024 indicated a general decreasing trend in the rainfall rate across most of the studied stations.

Table 3. Results of rainfall temporal trend in the study area (2001–2024)

Station	Kendall's τ	*z*-value	*p*-value	Trend	Sen's slope
Muthanna	−0.767	−5.044	0	decreasing	−2.003
Missan	−0.334	−2.192	0.02817	decreasing	−3.78
Basrah	−0.597	−3.962	0.00007	decreasing	−3.425
Thi Qar	−0.644	−4.278	0.00002	decreasing	−2.987
Qadissiya	−0.665	−4.411	0.00001	decreasing	−2.584
Babylon	−0.306	−2.007	0.04458	decreasing	−1
Kerbala	−0.071	−0.449	0.65333	no significant	−0.577
Wassit	−0.178	−1.162	0.24521	no significant	−2.817
Najaf	−0.665	−4.411	0.00001	decreasing	−1.322

The Muthanna, Missan, Basrah, Thi Qar, Qadissiya, Babylon, and Najaf stations exhibit negative Kendall's τ and *z*-values with statistically significant *p*-values ($p < 0.05$), confirming a significant downward trend in rainfall. In contrast, the Kerbala and Wassit stations illustrated no statistically significant trend ($p > 0.05$) despite having negative slope values. Furthermore, Sen's slope results reveal that all stations are characterized by declining rainfall rates of varying magnitudes, with the highest decreases observed in Missan, Basrah, and Thi Qar, and the lowest in Babylon, indicating an overall tendency toward reduced rainfall during the study period as shown Table 3 and Figure 15. With respect to spatial variability, the rainfall patterns display a gradual increase toward the eastern portions of the region, as shown in Figure 16.

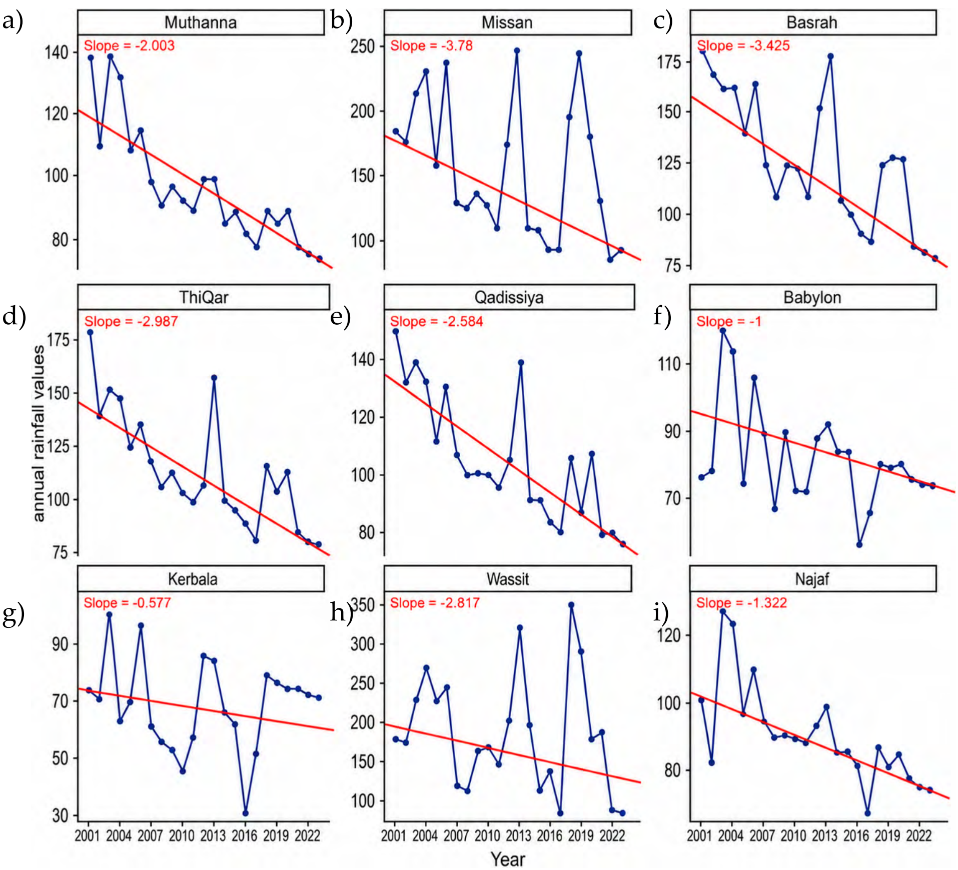

Fig. 15. Trend and temporal variability of rainfall rates over the governorates (2001–2024): a) Muthanna; b) Missan; c) Basrah; d) Thi Qar; e) Qadissiya; f) Babylon; g) Kerbala; h) Wassit; i) Najaf

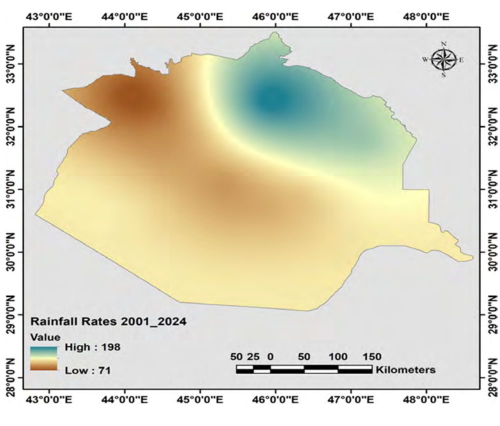

Fig. 16. Rainfall rate distribution over the study area (2001–2024)

Mean Temperature Dynamic

The results of the mean temperature trend during the period 2001–2024 indicated a general increasing trend across most stations: Muthanna, Missan, Basrah, Thi Qar, Qadissiya, Babylon, Kerbala, and Najaf. The stations showed positive Kendall's τ and z-values with statistically significant p-values ($p < 0.05$), confirming a significant upward trend in temperature. Meanwhile, the Wassit station exhibited no statistically significant trend ($p > 0.05$), despite a very slight positive slope. Also, Sen's slope values demonstrated that all stations experienced rising temperatures at varying rates, with the highest increases were observed in the Muthanna and Thi Qar stations, and the lowest in the Wassit and Babylon stations, indicating an overall warming trend in the region during the study period (Table 4, Fig. 17). Lower temperatures occurred in the eastern areas, increasing toward the western areas in the study area (Fig. 18).

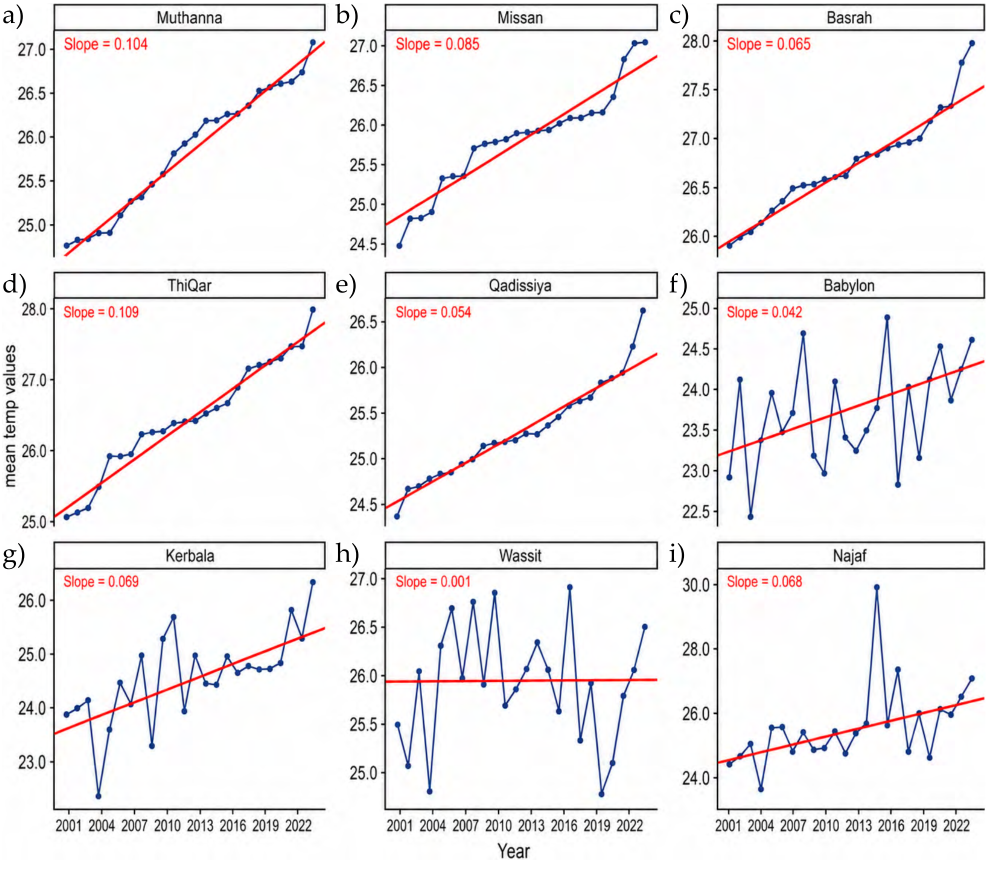

Fig. 17. Trend and temporal variability of mean temperature over the governorates (2001–2024): a) Muthanna; b) Missan; c) Basrah; d) Thi Qar; e) Qadissiya; f) Babylon; g) Kerbala; h) Wassit; i) Najaf

Table 4. Results of mean temperature temporal trend in the study area (2001–2024)

Station	Kendall's τ	*z*-value	*p*-value	Trend	Sen's slope
Muthanna	0.998	6.796	0	increasing	0.104
Missan	1	6.821	0	increasing	0.085
Basrah	1	6.821	0	increasing	0.065
Thi Qar	0.998	6.796	0	increasing	0.109
Qadissiya	0.998	6.796	0	increasing	0.054
Babylon	0.304	2.059	0.03952	increasing	0.042
Kerbala	0.507	3.448	0.00057	increasing	0.069
Wassit	0.011	0.050	0.96042	no significant	0.001
Najaf	0.464	3.150	0.00163	increasing	0.068

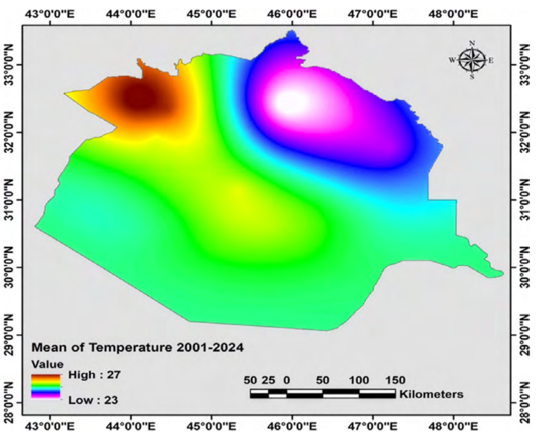

Fig. 18. Mean temperature distribution over the study area (2001–2024)

Land Surface Temperature (LST) Trend

The results of the mean LST showed a predominantly increasing trend across the stations. The Muthanna, Missan, Basrah, Thi Qar, Qadissiya, Wassit, and Najaf stations exhibit near-perfect positive Kendall's τ values with high *z*-statistics, with statistical significance ($p < 0.05$), indicating a significant upward trend in LST. Meanwhile, the Kerbala and Babylon stations showed no statistically significant trend ($p > 0.05$) despite having positive slope values. Sen's slope estimates further confirmed that all stations were experiencing increasing LST at varying rates, with the highest increases recorded in Muthanna and Najaf and the lowest in Babylon, as illustrated in Table 5 and Figures 19 and 20.

Table 5. Results of mean LST temporal trend in the study area (2001–2024)

Station	Kendall's τ	*z*-value	*p*-value	Trend	Sen's slope
Muthanna	1	6.655	0	increasing	0.205
Missan	1	6.655	0	increasing	0.144
Basrah	1	6.655	0	increasing	0.163
Thi Qar	1	6.655	0	increasing	0.179
Qadissiya	1	6.655	0	increasing	0.096
Babylon	0.075	0.475	0.63451	no significant	0.023
Kerbala	0.257	1.690	0.09098	no significant	0.068
Wassit	1	6.655	0	increasing	0.113
Najaf	1	6.655	0	increasing	0.240

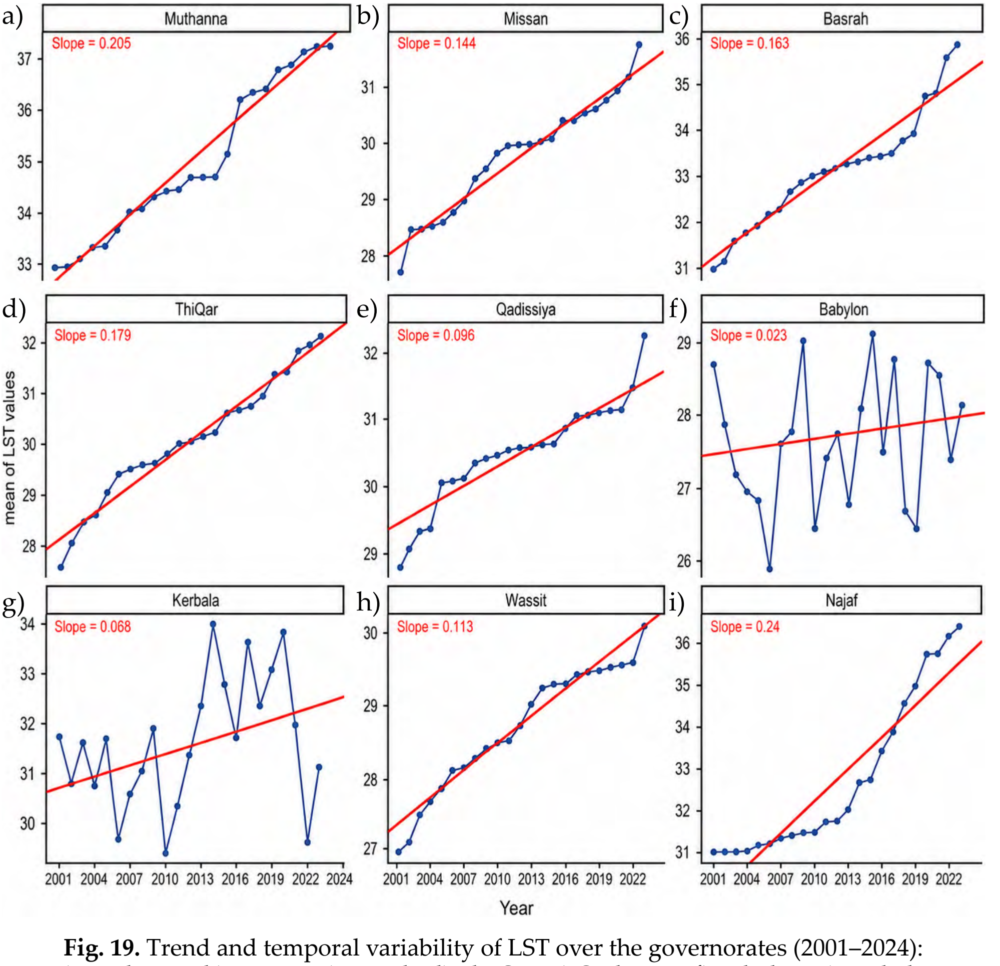

Fig. 19. Trend and temporal variability of LST over the governorates (2001–2024): a) Muthanna; b) Missan; c) Basrah; d) Thi Qar; e) Qadissiya; f) Babylon; g) Kerbala; h) Wassit; i) Najaf

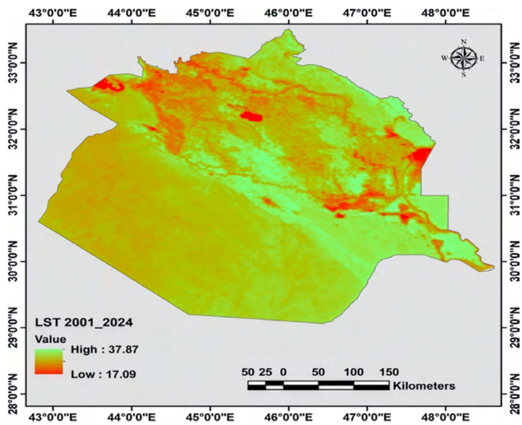

Fig. 20. Mean LST distribution over the study area (2001–2024)

Evaporation Pattern

The results for mean evaporation indicated a predominantly increasing trend across several stations during the period 2001–2024. The Muthanna, Missan, Basrah, Thi Qar, and Babylon stations exhibited positive Kendall's τ and *z*-values with statistical significance ($p < 0.05$), confirming a significant upward trend in evaporation. In contrast, the Qadissiya, Kerbala, and Wassit stations showed no statistically significant trends ($p > 0.05$), despite Kerbala and Qadissiya having slight positive slopes and the Wassit station having a negative slope. Sen's slope values further indicated that most stations are experiencing increasing evaporation rates, with the highest increases recorded in Muthanna and Basrah, while the lowest values are recorded in Qadissiya and Kerbala, reflecting an overall tendency toward increased evaporation rates during the study period, as shown in Table 6 and Figure 21. The spatial distribution of the evaporation indicated elevated rates in the western part of the study area, with a gradual decline toward the eastern parts, as shown in Figure 22.

Table 6. Results of mean evaporation trend in the study area (2001–2024)

Station	Kendall's τ	*z*-value	*p*-value	Trend	Sen's slope
Muthanna	1	6.821	0	increasing	5.002
Missan	1	6.821	0	increasing	2.416
Basrah	0.995	6.747	0	increasing	5.789
Thi Qar	0.355	2.406	0.01613	increasing	3.148
Qadissiya	0.163	1.091	0.27495	no significant	0.460
Babylon	1	6.821	0	increasing	2.380
Kerbala	0.036	0.223	0.82335	no significant	0.319
Wassit	−0.203	−1.364	0.17249	no significant	−2.003
Najaf	1	6.821	0	increasing	6.898

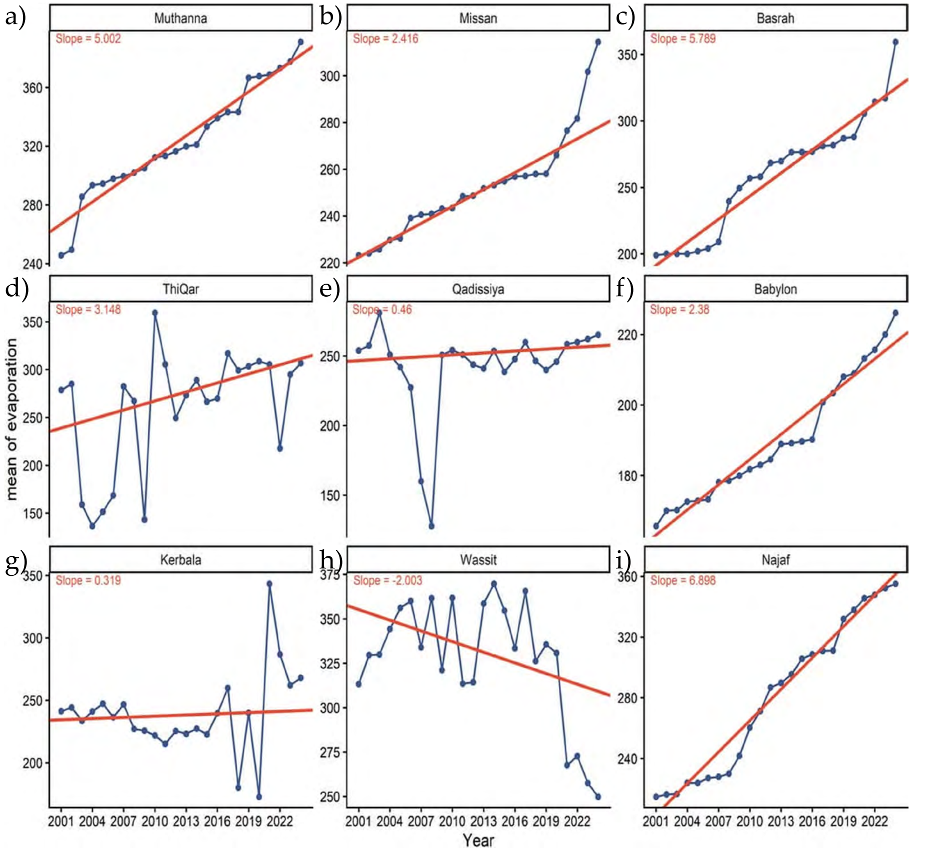

Fig. 21. Trend and temporal variability of evaporation over the governorates (2001–2024): a) Muthanna; b) Missan; c) Basrah; d) Thi Qar; e) Qadissiya; f) Babylon; g) Kerbala; h) Wassit; i) Najaf

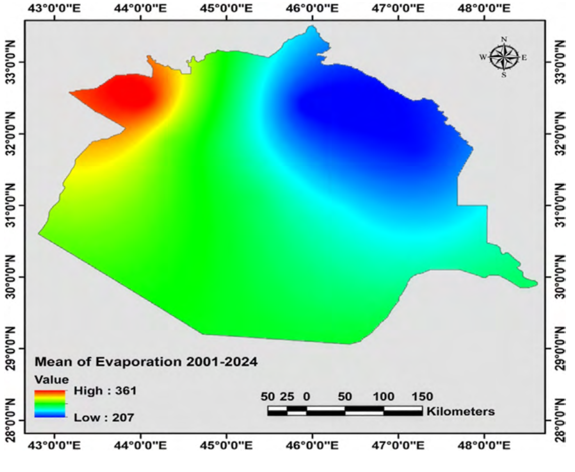

Fig. 22. Mean of evaporation distribution over the study area (2001–2024)

Relative Humidity Trends

The statistical results of the mean relative humidity during the period 2001–2024 indicated a general decreasing trend across several stations. The Muthanna, Missan, Basrah, Thi Qar, Babylon, and Kerbala stations exhibited negative Kendall's τ and *z*-values with statistical significance ($p < 0.05$), confirming a significant decrease in relative humidity. In contrast, the Najaf, Wassit, and Qadissiya stations showed no statistically significant trends ($p > 0.05$), despite slight positive or negative slope values. Sen's slope estimates further indicated that most stations were experiencing decreasing humidity at varying rates, with the most pronounced declines observed in Missan and Thi Qar, while the lowest changes were recorded in Najaf and Wassit, indicating an overall tendency toward decreased relative humidity during the study period, as illustrated in Table 7 and Figure 23. The spatial patterns of relative humidity showed a pronounced north–south gradient over the study region, characterized by lower values in the southern parts and a gradual increase toward the northern parts (Fig. 24).

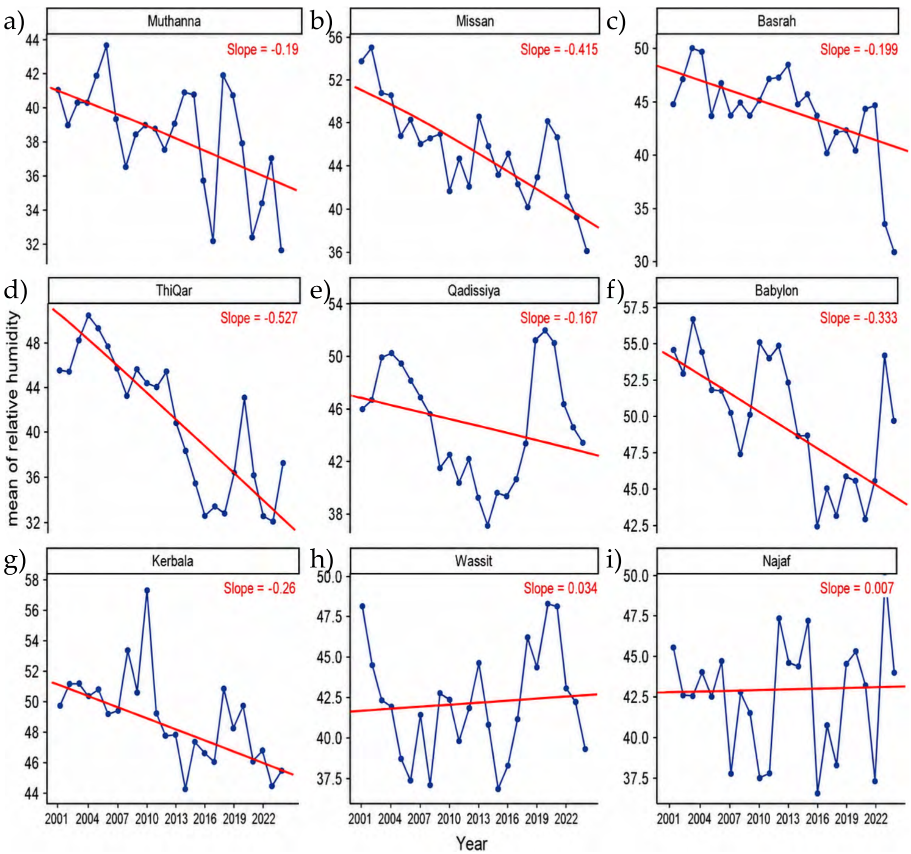

Fig. 23. Trend and temporal variability of relative humidity over the governorates (2001–2024): a) Muthanna; b) Missan; c) Basrah; d) Thi Qar; e) Qadissiya; f) Babylon; g) Kerbala; h) Wassit; i) Najaf

Table 7. Results of relative humidity trend in the study area (2001–2024)

Station	Kendall's τ	*z*-value	*p*-value	Trend	Sen's slope
Muthanna	−0.394	−2.654	0.00788	decreasing	−0.190
Missan	−0.599	−4.068	0.00005	decreasing	−0.415
Basrah	−0.456	−3.051	0.00221	decreasing	−0.199
Thi Qar	−0.679	−4.589	0	decreasing	−0.527
Qadissiya	−0.109	−0.719	0.47194	no significant	−0.167
Babylon	−0.455	−3.076	0.00208	decreasing	−0.333
Kerbala	−0.502	−3.398	0.00067	decreasing	−0.260
Wassit	0.054	0.347	0.72831	no significant	0.034
Najaf	0.015	0.074	0.94061	no significant	0.007

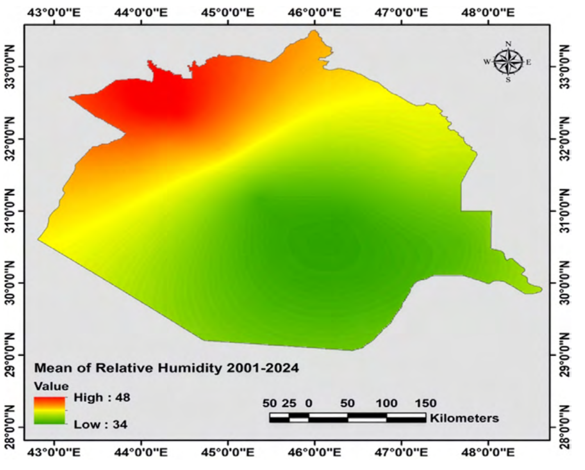

Fig. 24. Mean of relative humidity distribution over the study area (2001–2024)

Dust Storm Activity

The results of the mean dust storms indicated a statistically significant increasing trend across all the studied stations from 2001 to 2024. All stations showed high positive Kendall's τ values along with large *z*-statistics and highly significant *p*-values, confirming a strong upward trend in the frequency of dust storms. Sen's slope values further demonstrated that dust storms were increasing at varying rates, with the highest rates observed in Muthanna, Kerbala, Basrah, Thi Qar, and Najaf, while relatively lower increases were observed in Missan and Wassit. Generally, the results clearly showed dust storm activity throughout the study period, as shown in Table 8 and Figure 25. The dust storm activity displays a distinct west–east spatial gradient over the study area, with higher intensity observed in the western parts and progressively lower intensity toward the eastern parts (Fig. 26).

Table 8. Results of dust storms trend in the study area (2001–2024)

Station	Kendall's τ	*z*-value	*p*-value	Trend	Sen's slope
Muthanna	0.959	6.276	0	increasing	0.500
Missan	0.919	5.755	0	increasing	0.250
Basrah	0.919	5.755	0	increasing	0.500
Thi Qar	0.948	6.127	0	increasing	0.500
Qadissiya	0.919	5.755	0	increasing	0.425
Babylon	0.931	5.903	0	increasing	0.250
Kerbala	0.925	5.829	0	increasing	0.538
Wassit	0.933	5.928	0	increasing	0.171
Najaf	0.950	6.151	0	increasing	0.500

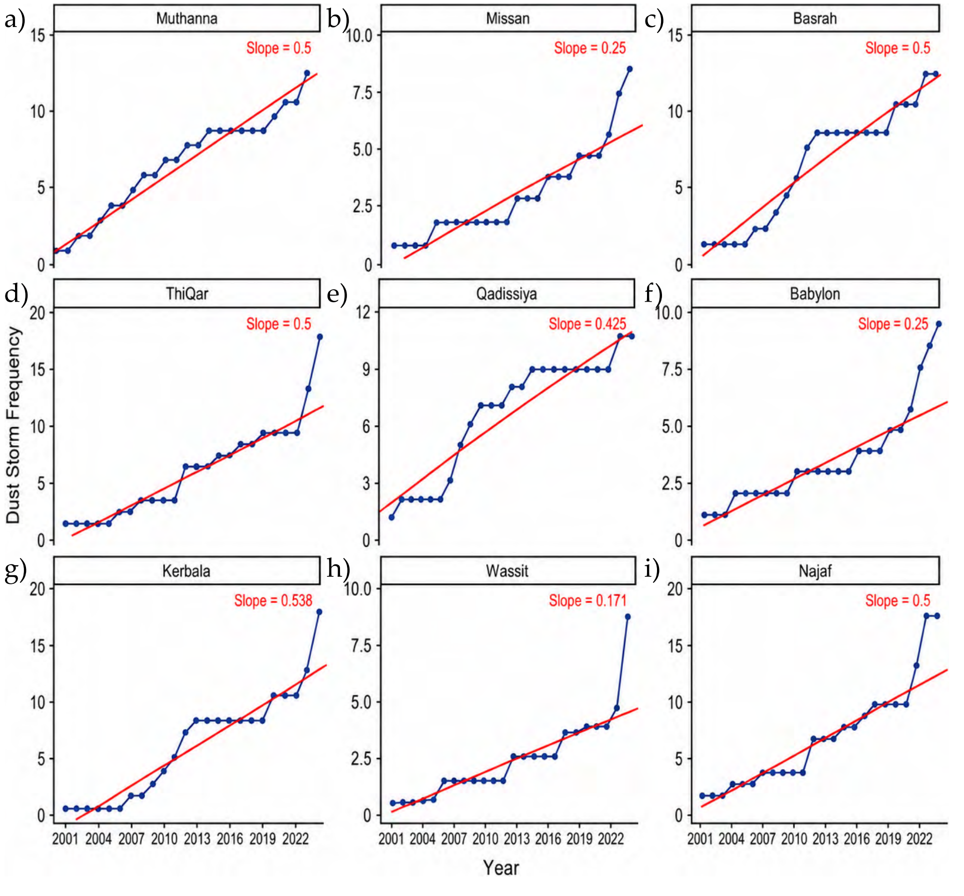

Fig. 25. Trend and temporal variability of dust storms over the governorates (2001–2024): a) Muthanna; b) Missan; c) Basrah; d) Thi Qar; e) Qadissiya; f) Babylon; g) Kerbala; h) Wassit; i) Najaf

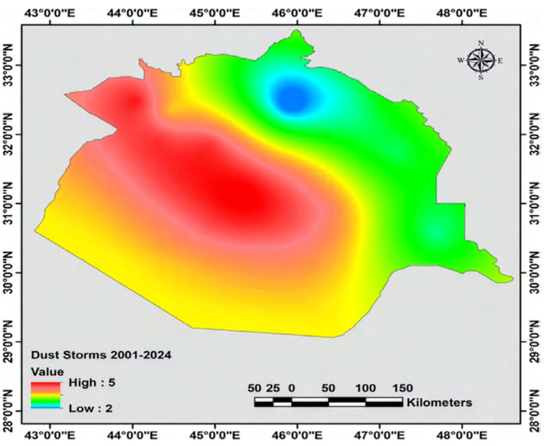

Fig. 26. Dust storm distribution over the study area (2001–2024)

Wind Speed Variability

The statistical results for mean wind speed indicated a generally increasing trend in most of the studied stations from 2001 to 2024. The Thi Qar, Missan, Qadissiya, Babylon, Kerbala, Wassit, and Najaf stations showed high positive Kendall's τ and z-values with statistical significance ($p < 0.05$), confirming a significant upward trend in the mean of the wind speed. On the other hand, the Basrah and Muthanna stations showed no statistically significant trends ($p > 0.05$) despite slight positive slope values. Sen's slope estimates further indicated that wind speed was increasing at varying rates, with the highest increase recorded in Missan and Wassit, while the lowest changes were observed in Basrah and Muthanna, indicating an overall tendency toward increasing wind speed during the study period, as illustrated in Table 9 and Figure 27. The wind speed patterns demonstrated a clear west–east gradient over the study region, with higher levels prevailing in the western parts and gradually diminishing toward the eastern parts, as presented in Figure 28.

Table 9. Results of wind speed trend in the study area (2001–2024)

Station	Kendall's τ	z-value	p-value	Trend	Sen's slope
Muthanna	0.105	0.695	0.48722	no significant	0.02
Missan	0.998	6.796	0	increasing	0.087
Basrah	0.076	0.496	0.61972	no significant	0.02
Thi Qar	0.993	6.722	0	increasing	0.05
Qadissiya	0.996	6.772	0	increasing	0.044
Babylon	0.998	6.796	0	increasing	0.045
Kerbala	0.996	6.772	0	increasing	0.043
Wassit	0.996	6.772	0	increasing	0.095
Najaf	0.998	6.796	0	increasing	0.039

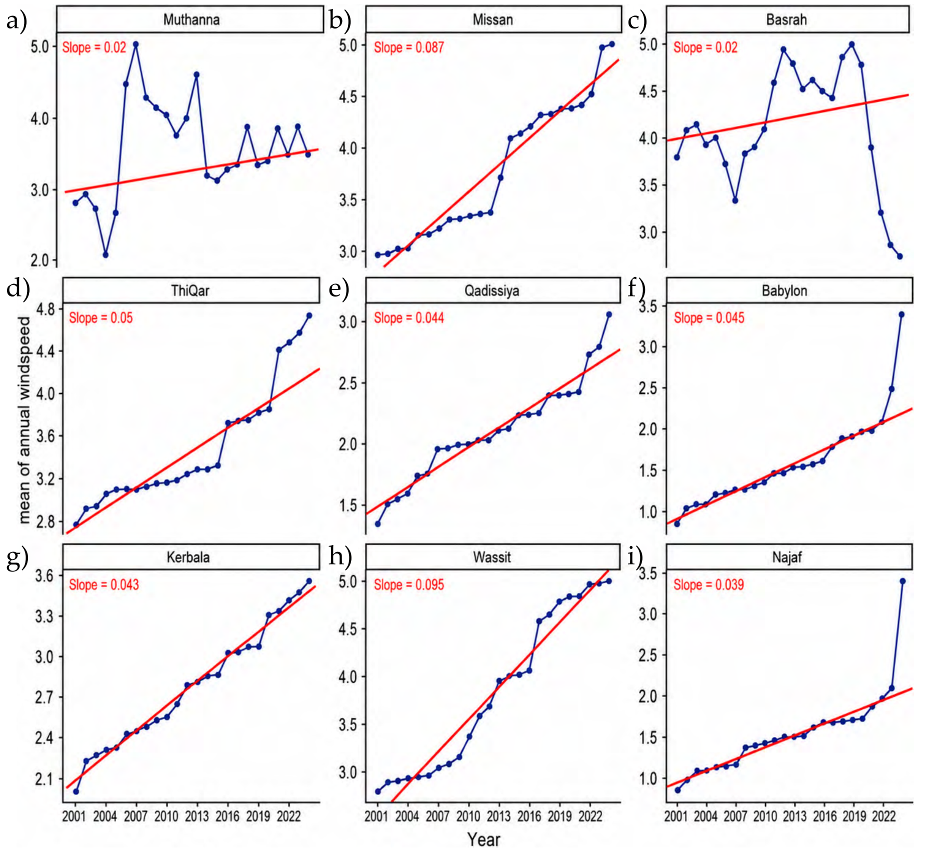

Fig. 27. Trend and temporal variability of wind speed over the governorates (2001–2024): a) Muthanna; b) Missan; c) Basrah; d) Thi Qar; e) Qadissiya; f) Babylon; g) Kerbala; h) Wassit; i) Najaf

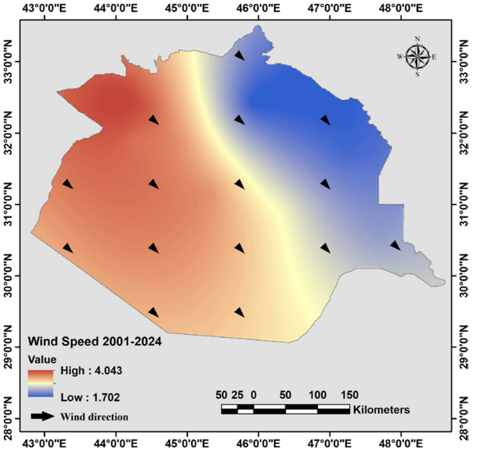

Fig. 28. Wind speed and direction over the study area (2001–2024)

Vegetation Condition and Drought Severity

VCI data for 2001–2012, and 2012–2024 revealed that extremely drought-affected areas increased from 60,789.597 km^2 (37%) in 2001–2012 to 71,000 km^2 (43%) in 2012–2024, while severely drought-affected areas decreased slightly from 57,894 km^2 (35%) to 53,000 km^2 (32%). The areas affected by moderately drought maintained approximately the same ratio of 23,539 km^2 (14%) to 23,590 km^2 (14%), and mildly drought-affected areas decreased from 15,284 km^2 (9%) to 13,000 km^2 (8%). In contrast, areas with no drought conditions dropped significantly from 7,775 km^2 (5%) in 2001–2012 to 4,692 km^2 (3%) in 2012–2024, indicating a clear shift toward more severe drought conditions, as shown in Figures 29 and 30.

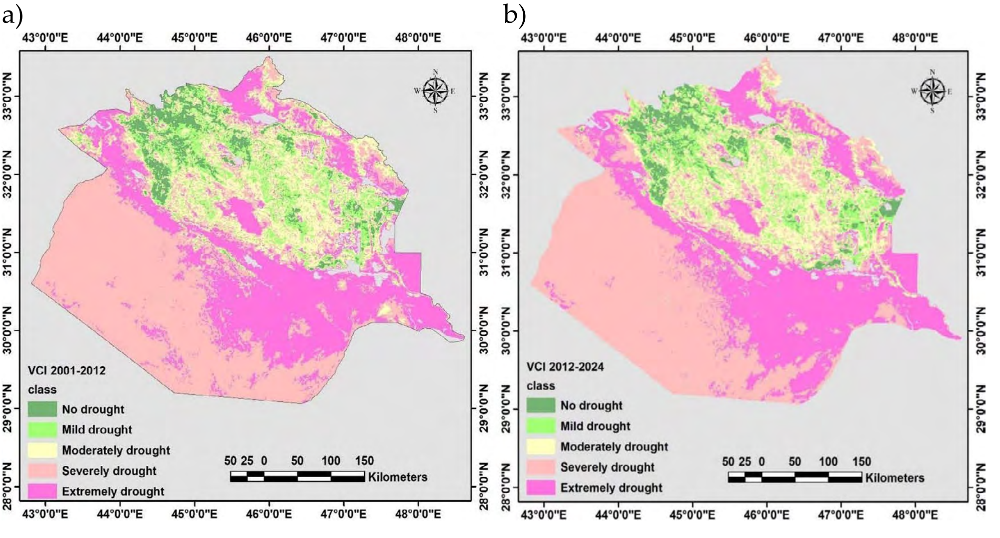

Fig. 29. Spatial distribution of drought over the study area:
a) 2001–2012; b) 2012–2024

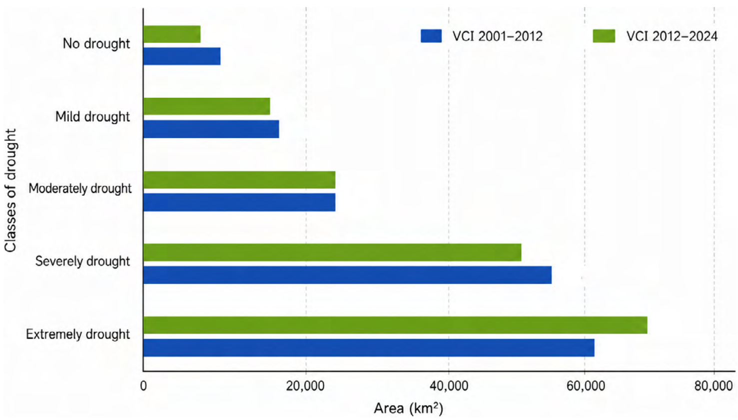

Fig. 30. Area of drought classes in the study area across two periods spanning 2001–2024

Surface Water Dynamics

The NDWI results revealed a clear and persistent downward trend in surface water extent throughout the study period, with the total area declining from 36,692 km² (22%) in 2001–2012 to 25,275 km² (15%) in 2012–2024, indicating a continuous reduction in surface water coverage over time, as shown in Figures 31 and 32.

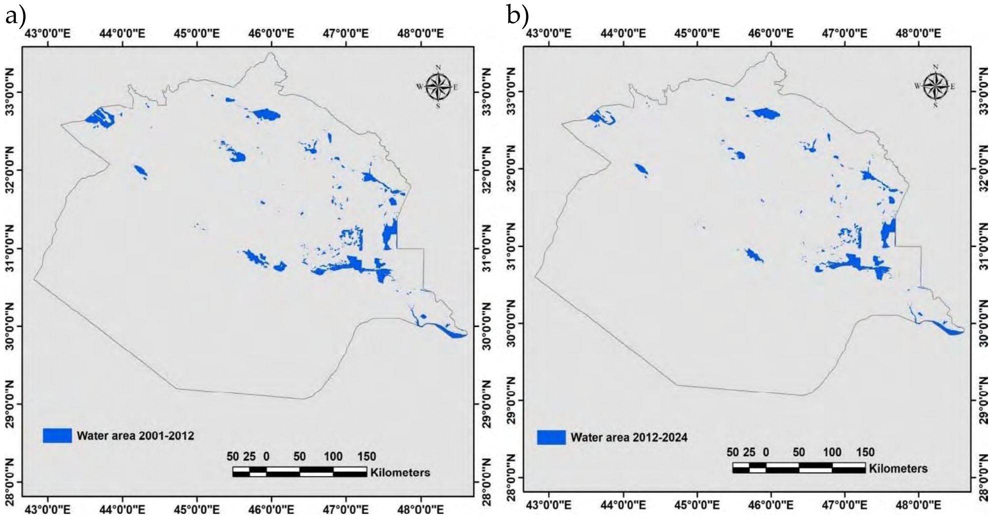

Fig. 31. Spatial distribution of water cover over the study area: a) 2001–2012; b) 2012–2024

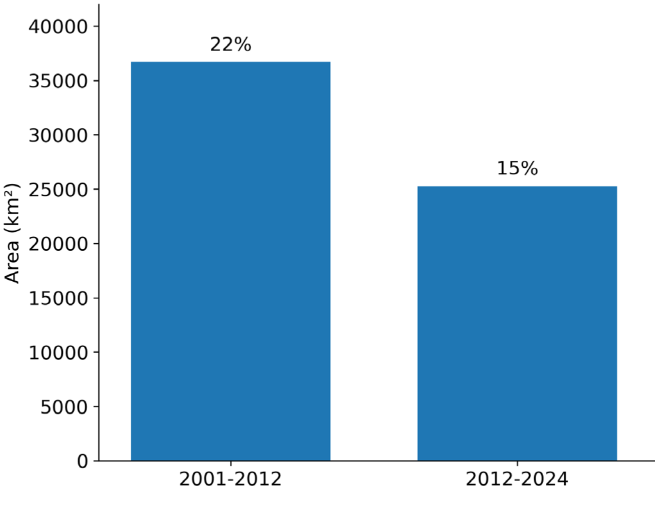

Fig. 32. Area of water cover in the study area across two periods spanning 2001–2024

6. Discussion

This study indicated that the study area has experienced significant and accelerating climate and environmental changes over the period (2001–2024), reflecting a clear transition toward hotter and drier conditions that can be interpreted within the framework of ongoing drought. The Mann–Kendall test and Sen's slope estimator revealed a statistically significant decreasing trend in rainfall across most stations, particularly in Missan, Basrah, and Thi Qar, while non-significant negative trends were observed in Kerbala and Wassit. The reduction in rainfall rates was the main driver of environmental changes, starting from limited water availability that reduces soil moisture and thus vegetation cover. While there was some spatial variability indicating slightly more rainfall over the eastern parts of the region, these observations were consistent with an overall decreasing temporal trend in rainfall.

At the same time, the results also showed a statistically significant increase in air temperature at most stations and an unequivocal rise in LST. This warming trajectory indicates a rise in the thermal energy of the system, thereby enhancing evapotranspiration processes and elevating water demand. Accordingly, the study indicated growing evaporation at many stations, especially in Muthanna and Basrah, and a regionally decreasing relative humidity over time. This combination clearly demonstrates a poor hydrological status, with loss through evaporation greater than replenishment by rainfall, and hence progressive soil drying leading to lessening water storage capacity. This is consistent with the study by Khalbas and Kadhum [41].

The degradation of vegetation cover further supports this interpretation. The VCI results indicated a marked increase in regions affected by extreme drought during the period from 2001 to 2024, while regions classified as non-drought decreased during the same period. These results refer to a substantial degradation in vegetation cover and a reduced ability of ecosystems to recover from climatic stress. This decrease is closely linked to decreased rainfall, raised temperatures, and increased evaporation, all of which engage with vegetation stress and decreased biomass productivity. This is consistent with the study by Liu et al. [42].

Furthermore, the NDWI results illustrated a continuous decrease in surface water area during the period from 2001 to 2024. This reduction reflects the combined effects of decreased rainfall, increased temperature, and reduced river levels, leading to declined surface water resources. The lack of surface water not only affects the hydrological balance but also places additional stress on ecological and agricultural systems in the study area. This dynamic aligns with the outcomes of Bhaga et al. [43], who indicated that climate change and recurring droughts have placed immense pressure on water resources in most parts of the world, particularly arid and semi-arid regions, which have been the most affected. These impacts have been especially pronounced on surface water resources.

Environmental stresses are also aggravated in the region by decreasing inflows from the Euphrates and Tigris rivers, caused mainly by water regulation upstream of those watersheds and dam construction within neighboring countries that drastically decreased the water availability, further exacerbating climatic variability and drought impacts in the region. This is consistent with the findings of Al-Ansari [44], which confirmed that the policies of upstream countries (Iran and Turkey) represent an important factor in the deterioration of the environmental situation in the region.

The study also showed that all stations indicated a robust and statistically significant increase in dust storm activity along with raised wind speeds over most parts of the study area, which is consistent with the study by Al Ameri et al. [45].

The results indicated the existence of a positive feedback mechanism where decreased vegetation cover and soil moisture leave the Earth's surface exposed, making it more vulnerable to wind erosion. Higher winds produce more dust by lifting it off the ground, resulting in an increased frequency and intensity of storms. Consequently, these storms lead to the loss of fine soil particles, which are essential for developing fertile ground and vegetation growth, contributing positively toward land degradation processes.

Overall, the outcomes highlight a tightly interconnected system in which environmental and climatic variables interact in a cascading manner. Decreasing rainfall leads to a series of processes, including increasing temperatures, raising evaporation, reduced relative humidity, soil moisture depletion, vegetation cover degradation, reduced surface water, and increased dust storm activity. This series of interactions indicates that the observed changes are not isolated phenomena but components of an integrated environmental shift. Consequently, central and southern Iraq are undergoing a clear transition toward a more arid and fragile environmental condition due to coupled climate and land surface feedback mechanisms, underscoring the need for adaptive strategies to manage water resources and mitigate or treat land degradation under changing hydrological and climatic conditions.

7. Conclusions

This study hypothesized that the study area has transitioned to greater aridity and environmental susceptibility, with climatic changes as a primary driver of increases in drought and ecological deterioration. The results supported this hypothesis and indicated that the central and southern Iraq region has been subjected to significant environmental and climatic changes during the period from 2001 to 2024, indicating a clear shift toward increasingly arid conditions. The outcomes showed a statistically significant decrease in rainfall rate over most stations, accompanied by rising LST and air temperature, which together increased evaporation rates and decreased the relative humidity. This combination created a persistent imbalance in the hydrological system, leading to decreasing soil moisture and increasing environmental stress. The analysis of vegetation conditions indicated a substantial increase in regions affected by extreme drought from 37 to 43%, alongside a marked reduction in areas with no drought from 5 to 3%, reflecting decreasing ecosystem health. Similarly, surface water dynamics indicated a continuous decrease in surface water extent from 22 to 15%, due to reduced rainfall and increased evaporation. These pressures are further increased by reduced inflows from the Tigris and Euphrates rivers due to upstream water regulation, which has limited the region's ability to compensate for climatic variability. Furthermore, the increasing wind speed and frequency of dust storms highlighted a reinforcing cycle of land degradation in the region, where vegetation loss and soil exposure enhance the susceptibility to erosion. The results confirmed an ongoing process of drought, emphasizing the need for sustainable water and land management strategies in the study area.

Funding

This research received no specific grant from any funding agency in the public, commercial, or not-for-profit sectors.

CRediT Author Contribution

A.G.K.: project administration, conceptualization, writing – original draft, software, formal analysis, visualization.

R.A.A: data curation, writing, review and editing.

I.A.A.: visualization, review and editing, supervision.

A.T.Z.: visualization, review and editing, supervision.

Declaration of Competing Interests

The authors declare that they have no known competing financial interests or personal relationships that could have appeared to influence the work reported in this paper.

Data Availability

The data that support the findings of this study are available from the authors upon reasonable request.

Use of Generative AI and AI-Assisted Technologies

No generative AI or AI-assisted technologies were employed in the preparation of this manuscript.

Acknowledgements

The authors acknowledge the Scientific Research Commission for providing the necessary research facilities.

References

[1] Mohammed A.S., Alhadeethi I.K., Al-Hadeethi B., Almawla A.S.: *Assessing the impact of climate change on temperature and rainfall patterns in Iraq's northern desert using GIS*. International Journal of Design & Nature and Ecodynamics, vol. 20(5), 2025, pp. 1151–1159. https://doi.org/10.18280/ijdne.200519.

[2] UNESCO: *Integrated drought risk management, DRM: National framework for Iraq: An analysis report* (2nd ed.). UNESCO Office for Iraq, 2014. https://unesdoc.unesco.org/ark:/48223/pf0000228343.locale=en [access: November 10, 2025].

[3] Hashim B.M., Al Maliki A., Abd Alraheem E., Al-Janabi A.M.S., Halder B., Yaseen Z.M.: *Temperature and precipitation trend analysis of the Iraq region under SRES scenarios during the twenty-first century*. Theoretical and Applied Climatology, vol. 148(3–4), 2022, pp. 881–898. https://doi.org/10.1007/s00704-022-03976-y.

[4] Jamal J.H., Abbas H.W., Ali K.Z., Mahmood S.: *Applications of remote sensing and GIS in assessing climate change and forecasting air quality in Iraq*. Journal of Engineering and Technology Development, vol. 1(1), 2023, pp. 1–7.

[5] Sultan M.A., Hashim B.M., Hassan A.R., Nasser M.H.: *Determination of impacts of climate change on temperature and rainfall variations in some southern Iraqi governorate using GIS*. Iraq Geological Survey, vol. 19(2), 2023, pp. 151–166. https://doi.org/10.59150/ibgm1902a011.

[6] Al-Timimi Y.K., Osamah O.A.: *Comparative study of four meteorological drought indices in Iraq*. Journal of Applied Physics (IOSR-JAP), vol. 8(5), 2016, pp. 76–84.

[7] Osamah O.A.: *Comparative Analysis of Some Drought Indices in Iraq* [MSc thesis]. Department of Atmospheric Sciences, College of Science, Al-Mustansiriyah University, Iraq 2017.

[8] Sholihah R.I., Trisasongko B.H., Shiddiq D., Iman L.O.S., Kusdaryanto S., Manijo, Panuju D.R.: *Identification of agricultural drought extent based on vegetation health indices of Landsat data: Case of Subang and Karawang, Indonesia*. Procedia Environmental Sciences, vol. 33, 2016, pp. 14–20. https://doi.org/10.1016/j.proenv.2016.03.051.

[9] Abood R.H., Mahdi A.H., Khalaf A.G., Kadhim A.A.: *Evaluation of land cover changes in Karbala governorate using remote sensing and GIS techniques*. Iraqi National Journal of Earth Sciences, vol. 24(2), 2024, pp. 177–185. https://doi.org/10.33899/earth.2023.143323.1144.

[10] Al-Timimi Y.K., Al-Khudhairy A.A.: *Spatial and temporal analysis of maximum temperature over Iraq*. Al-Mustansiriyah Journal of Science, vol. 29(1), 2018, pp. 1–8. http://doi.org/10.23851/mjs.v29i1.257.

[11] Mzuri R.T., Omar A.A., Mustafa Y.T.: *Spatiotemporal analysis of vegetation cover and its response to terrain and climate factors in Duhok governorate, Kurdistan region, Iraq*. Iraqi Geological Journal, vol. 54(1A), 2021, pp. 161–176. https://doi.org/10.46717/igj.54.1A.10Ms-2021-01-31.

[12] Aljuhaishi S., Al-Timimi Y., Wahab B.: *Spatio-temporal variation of weather systems and their seasonal variability in Iraq*. Iraqi National Journal of Earth Sciences, vol. 25(4), 2025, pp. 260–272. https://doi.org/10.33899/earth.2024.153466.1352.

[13] Al-Maliki L.A., Mukheef R.A.A.H., El-Tawil K., Al-Ansari N.: *Climate change trends and adaptation strategies in southern regions of Iraq*. Journal of Groundwater Science and Engineering, vol. 13(4), 2025, pp. 449–468. https://doi.org/10.26599/JGSE.2025.9280065.

[14] Ali Muter S., Al-Jiboori M.H., Al-Timimi Y.K.: *An assessment the correlation between rainfall and normalized difference vegetation index (NDVI) over Iraq*. Italian Journal of Agrometeorology, no. 2, 2025, pp. 79–94. https://doi.org/10.36253/ijam-3069.

[15] Alemu W.G.: *Climate change, analysis of temperature and rainfall trend in northern Ethiopia: In the case of Dessie Zuria*. American Journal of Biological and Environmental Statistics, vol. 11(4), 2025, pp. 151–164. https://doi.org/10.11648/j.ajbes.20251104.11.

[16] Radić M., Šerić L., Bugarić M.: *Evaluation of spatial interpolation methods for wind speed and direction: A case study in Split-Dalmatia County*. International Archives of the Photogrammetry, Remote Sensing and Spatial Information Sciences, vol. XLVIII-4/W13-2025, 2025, pp. 193–200. https://doi.org/10.5194/isprs-archives-XLVIII-4-W13-2025-193-2025.

[17] Feng Z., Wang R., Liu X., Huang M., Huo L.: *Spatial interpolation methods of temperature data based on geographic information system – taking Jiangxi Province as an example*. MDPI Proceedings, vol. 110(1), 2024, 14. https://doi.org/10.3390/proceedings2024110014.

[18] Pandey N., Panwar K., Sharma M., Punia M.P.: *Analysis of spatial interpolation techniques for rainfall data using various methods: A case study of Bisalpur catchment area*. International Journal of Engineering Research & Technology (IJERT), vol. 4(23), 2016, IJERTCONV4IS23022.

[19] State Commission of Survey: *Iraq administrative map, scale 1:1,000,000*. State Commission of Survey, Baghdad 2010.

[20] NASA: *NASA Prediction of Worldwide Energy Resources (POWER)* [data base]. https://power.larc.nasa.gov [access: March 3, 2025].

[21] United States Geological Survey (USGS): *EarthExplorer* [search engine]. https://www.usgs.gov/tools/earthexplorer [access: March 5, 2025].

[22] Helmi A.M., Elgamal M., Farouk M.I., Abdelhamed M.S., Essawy B.T.: *Evaluation of geospatial interpolation techniques for enhancing spatiotemporal rainfall distribution and filling data gaps in Asir region, Saudi Arabia*. Sustainability, vol. 15(18), 2023, 14028. https://doi.org/10.3390/su151814028.

[23] El-Basir M.A.A., Hamed Y., Selim T., Berndtsson R., Helmi A.M.: *Developing rainfall spatial distribution for using geostatistical gap-filled terrestrial gauge records in the mountainous region of Oman*. Water, vol. 17(18), 2025, 2695. https://doi.org/10.3390/w17182695.

[24] Mohammed P.A., Al Nuaimy Q.A.M., Shareef M.A.: *Spatial distribution maps of soil chemical properties using kriging model and ArcGIS in Kirkuk City, Iraq*. Iraqi National Journal of Earth Sciences, vol. 25(4), 2025, pp. 231–245. https://doi.org/10.33899/earth.2024.153439.1351.

[25] Salehı M., Oral H.V.: *An example of kriging method based on environmental temperature for altitude mapping using ArcGIS software*. Gazi University Journal of Science Part A: Engineering and Innovation, vol. 10(4), 2023, pp. 392–401. https://doi.org/10.54287/gujsa.1339151.

[26] Batool A., Ahmad S., Waseem A., Kartal V., Ali Z., Mohsin M.: *Evaluating variogram models and kriging approaches for analyzing spatial trends in precipitation simulations from global climate models*. Acta Geophysica, vol. 73(10), 2025, pp. 3677–3697. https://doi.org/10.1007/s11600-025-01545-1.

[27] Jannah F.M., Fitriani R., Pramoedyo H.: *Spatio-temporal kriging for monthly precipitation interpolation in East Kalimantan*. Inferensi, vol. 8(2), 2025, pp. 119–128. https://doi.org/10.12962/j27213862.v8i2.22195.

[28] Jang D., Kim N., Choo H.: *Kriging interpolation for constructing database of the atmospheric refractivity in Korea*. Remote Sensing, vol. 16(13), 2024, 2379. https://doi.org/10.3390/rs16132379.

[29] Baniya B., Tang O., Xu X., Haile G.G., Shrestha G.C.: *Spatial and temporal variation of drought based on satellite derived vegetation condition index in Nepal from 1982–2015*. Sensors, vol. 19(2), 2019, 430. https://doi.org/10.3390/s19020430.

[30] Ghobadi M., Badehian Z.: *Assessment of agricultural drought severity using multi-temporal remote sensing data in Lorestan region*. Scientific Reports, vol. 15, 2025, 3087. https://doi.org/10.1038/s41598-025-03087-4.

[31] Latuamury B., Talaohu M., Sahusilawane F., Imlabla W.N.: *Correlation of normalized difference water index and base flow index in small island watershed landscapes*. IOP Conference Series: Earth and Environmental Science, vol. 883, 2021, 012072. https://doi.org/10.1088/1755-1315/883/1/012072.

[32] Ji L., Zhang L., Wylie B.: *Analysis of dynamic thresholds for the normalized difference water index*. Photogrammetric Engineering & Remote Sensing, vol. 75(11), 2009, pp. 1307–1317. https://doi.org/10.14358/PERS.75.11.1307.

[33] Ali S., Cheema M.J.M., Waqas M.M., Waseem M., Leta M.K., Qamar M.U., Awan U.K., Bilal M., Rahman M.H.: *Flood mitigation in the transboundary Chenab river basin: A basin-wise approach from flood forecasting to management*. Remote Sensing, vol. 13(19), 2021, 3916. https://doi.org/10.3390/rs13193916.

[34] Al-Saadi M.W.H.: *The effects of climate change on normalized difference vegetation index (NDVI) in the Al-Hawizeh Marsh*. International Journal of Environment and Climate Change, vol. 14(8), 2024, pp. 208–217. https://doi.org/10.9734/ijecc/2024/v14i84343.

[35] Aditya F., Gusmayanti E., Sudrajat J.: *Rainfall trend analysis using Mann-Kendall and Sen's slope estimator test in West Kalimantan*. IOP Conference Series: Earth and Environmental Science, vol. 893, 2021, 012006. https://doi.org/10.1088/1755-1315/893/1/012006.

[36] Aswad F.K., Yousif A.A., Ibrahim S.A.: *Trend analysis using Mann–Kendall and Sen's slope estimator test for annual and monthly rainfall for Sinjar District, Iraq*. Journal of University of Duhok, vol. 23(2), 2020, pp. 501–508. https://doi.org/10.26682/csjuod.2020.23.2.41.

[37] Gianquintieri L., Mahakalkar A.U., Caiani E.G.: *Exploring spatial–temporal patterns of air pollution concentration and their relationship with land use*. Atmosphere, vol. 15(6), 2024, 699. https://doi.org/10.3390/atmos15060699.

[38] Njeban H.S.: *Comparison and evaluation of GIS-based spatial interpolation methods for estimation groundwater level in AL-Salman district – southwest Iraq*. Journal of Geographic Information System, vol. 10(4), 2018, pp. 362–380. https://doi.org/10.4236/jgis.2018.104019.

[39] Moran P.A.P.: *Notes on continuous stochastic phenomena*. Biometrika, vol. 37(1/2), 1950, pp. 17–23. https://doi.org/10.2307/2332142.

[40] Fu W.J., Jiang P.K., Zhou G.M., Zhao K.L.: *Using Moran's I and GIS to study the spatial pattern of forest litter carbon density in a subtropical region of southeastern China*. Biogeosciences, vol. 11(9), 2014, pp. 2401–2409. https://doi.org/10.5194/bg-11-2401-2014.

[41] Khalbas M.I., Kadhum J.H.: *Impact of climate change on water contains for different vegetation cover areas in Wasit province during (1992–2024)*. Basrah Journal of Agricultural Sciences, vol. 38(2), 2025, pp. 352–365. https://doi.org/10.37077/25200860.2025.38.2.26.

[42] Liu J., Li M., Li R., Shalamzari M.J., Ren Y., Silakhori E.: *Comprehensive assessment of drought susceptibility using predictive modeling, climate change projections, and land use dynamics for sustainable management*. Land, vol. 14(2), 2025, 337. https://doi.org/10.3390/land14020337.

[43] Bhaga T.D., Dube T., Shekede M.D., Shoko C.: *Impacts of climate variability and drought on surface water resources in Sub-Saharan Africa using remote sensing: A review*. Remote Sensing, vol. 12(24), 2020, 4184. https://doi.org/10.3390/rs12244184.

[44] Al-Ansari N.: *Water resources in Iraq: Perspectives and prognosis*. Journal of Water Resources and Geosciences, vol. 4(1), 2025, pp. 249–266.

[45] Al Ameri I.D.S., Briant R.M., Engels S.: *Drought severity and increased dust storm frequency in the Middle East: A case study from the Tigris-Euphrates alluvial plain, Central Iraq*. Weather, vol. 74(12), 2019, pp. 416–426. https://doi.org/10.1002/wea.3445.